

Mid-IR and UV-Vis-NIR Mueller matrix ellipsometry characterization of tunable hyperbolic metamaterials based on self-assembled carbon nanotubes

Stefan Schöche, Po-Hsun Ho, John A. Roberts, Shangjie J. Yu, Jonathan A. Fan, and Abram L. Falk

Citation: *Journal of Vacuum Science & Technology B* **38**, 014015 (2020); doi: 10.1116/1.5130888

View online: <https://doi.org/10.1116/1.5130888>

View Table of Contents: <https://avs.scitation.org/toc/jvb/38/1>

Published by the [American Vacuum Society](#)

ARTICLES YOU MAY BE INTERESTED IN

[Imaging ellipsometry for curved surfaces](#)

Journal of Vacuum Science & Technology B **38**, 014016 (2020); <https://doi.org/10.1116/1.5129654>

[Spectral ellipsometry of monolayer transition metal dichalcogenides: Analysis of excitonic peaks in dispersion](#)

Journal of Vacuum Science & Technology B **38**, 014002 (2020); <https://doi.org/10.1116/1.5122683>

[Ultrasensitive broadband infrared 4 × 4 Mueller-matrix ellipsometry for studies of depolarizing and anisotropic thin films](#)

Journal of Vacuum Science & Technology B **38**, 014003 (2020); <https://doi.org/10.1116/1.5129800>

[In situ real-time and ex situ spectroscopic analysis of Al₂O₃ films prepared by plasma enhanced atomic layer deposition](#)

Journal of Vacuum Science & Technology B **38**, 014014 (2020); <https://doi.org/10.1116/1.5122797>

[Plasmonic coupling and how standard ellipsometry can feel surface plasmon](#)

Journal of Vacuum Science & Technology B **38**, 013603 (2020); <https://doi.org/10.1116/1.5122267>

[Brilliant mid-infrared ellipsometry and polarimetry of thin films: Toward laboratory applications with laser based techniques](#)

Journal of Vacuum Science & Technology B **37**, 060801 (2019); <https://doi.org/10.1116/1.5122869>



NEW

AVS Quantum Science

A new interdisciplinary home for impactful quantum science research and reviews

Co-Published by



NOW ONLINE

The banner features a dark blue background with a teal diagonal banner in the top left corner containing the word 'NEW'. The main title 'AVS Quantum Science' is in large white font, with the subtitle 'A new interdisciplinary home for impactful quantum science research and reviews' below it. The logos for 'AIP Publishing' and 'AVS' are shown on the left, and a teal button with 'NOW ONLINE' is on the right. The background is decorated with various circular icons representing quantum science concepts like atoms, molecules, and data plots.

Mid-IR and UV-Vis-NIR Mueller matrix ellipsometry characterization of tunable hyperbolic metamaterials based on self-assembled carbon nanotubes



Cite as: J. Vac. Sci. Technol. B 38, 014015 (2020); doi: 10.1116/1.5130888
Submitted: 7 October 2019 · Accepted: 27 December 2019 ·
Published Online: 16 January 2020



Stefan Schöche,¹ Po-Hsun Ho,² John A. Roberts,² Shangjie J. Yu,² Jonathan A. Fan,²  and Abram L. Falk³ 

AFFILIATIONS

¹J.A. Woollam Co., Inc., 645 M St., Suite 102, Lincoln, Nebraska 68508

²Stanford University, 348 Via Pueblo, Spilker Building, Room 307, Stanford, California 94305-4088

³IBM T.J. Watson Research Center, 1101 Kitchawan Road, Yorktown Heights, New York 10598

Note: This paper is part of the Conference Collection: 8th International Conference on Spectroscopic Ellipsometry 2019, ICSE.

ABSTRACT

Mueller matrix ellipsometry over the wide spectral range from the mid-IR to UV is applied to characterize the dielectric function tensor for films of densely packed single-walled carbon nanotubes aligned in the surface plane. These films optically act as metamaterials with an in-plane anisotropic, bulk effective medium response. A parameterized oscillator model is developed to describe electronic interband transitions, $\pi - \pi^*$ plasmon resonances, and free-carrier absorption. Wide ranges of hyperbolic dispersion are observed and exceptional tuneability of the hyperbolic ranges is demonstrated by comparing results for a film of aligned but unordered carbon nanotubes with a film fabricated under optimized conditions to achieve hexagonally close-packed alignment of the nanotubes. The effect of doping on the optical properties and hyperbolic range is discussed.

Published under license by AVS. <https://doi.org/10.1116/1.5130888>

I. INTRODUCTION

Hyperbolic metamaterials (HMM) were proposed as a multifunctional platform to realize waveguiding, imaging, sensing, and quantum and thermal engineering beyond conventional device performance.¹ HMMs display hyperbolic (or indefinite) dispersion, which originates from one of the principal components of their electric or magnetic effective tensor having the opposite sign to the other two principal components. Type-I HMMs have one negative component of the dielectric tensor ($\epsilon_{zz} < 0$; $\epsilon_{xx}, \epsilon_{yy} > 0$), while Type-II HMMs have two negative components ($\epsilon_{xx}, \epsilon_{yy} < 0$; $\epsilon_{zz} > 0$). Traditionally, HMMs are formed by combining a metallic and dielectric building block, either as thin sheets (Type-II) or metal nanorods embedded in a dielectric matrix (Type-I).² However, these materials have fixed hyperbolic spectral ranges and are not dynamically tunable.

In this paper, we demonstrate a novel approach to form Type-I HMMs based on carbon nanotubes (CNTs). The one-dimensional character of electrons, phonons, and excitons in individual single-walled CNTs leads to extremely anisotropic electronic, thermal, and optical properties. Recently, the preparation of large-scale

monodomain films of aligned single-walled CNT using slow-vacuum filtration was demonstrated.³ A refinement of this technique showed that nanotubes in these films can be aligned and crystallized into two-dimensional ordered arrays with domain sizes of approximately 25 nm.⁴ Control of the doping level and various grating methods lead to highly tunable optical properties. We recently demonstrated that densely packed CNT films optically act as a metamaterial with an in-plane anisotropic, bulk effective medium response.⁵ Hyperbolic modes confined in nanoribbon resonators with differing widths and orientations relative to the nanotube were shown to support strong light localization. In order to predict and tune the optical behavior of these nanoribbon resonators, the hyperbolic spectral ranges in the dielectric function tensor of bulk CNT films need to be determined.

Early publications reported intrinsic uniaxial behavior in CNTs aligned within the surface plane.^{6,7} The Maxwell-Garnett effective medium approximation utilizing the dielectric function tensor components of graphite proved to be insufficient to correctly describe the experimentally observed dielectric function tensor component perpendicular to the CNT axes. A similar discrepancy

was found when applying effective medium approximations to the vertically aligned CNT (Ref. 8) and randomly oriented bundles of CNTs.⁹ Early theoretical studies confirmed that effective medium theories will work to some extent in films containing isolated CNTs but fail to correctly describe densely packed films due to neglect of the effect of the diameter-dependent curvature in the CNT and the interaction between densely packed nanotubes.^{10,11} Detailed calculations considering the geometry of the CNT based on $\mathbf{k}\cdot\mathbf{p}$ theory,^{12,13} tight-binding models,^{14,15} or density functional theory^{16,17} successfully described the optical response of CNT films and confirmed that the optical response parallel and perpendicular to the CNT axes must be described independently. The diameter and helical arrangement of the CNT were predicted to strongly influence the electronic character and observed optical absorption. Armchair CNTs were demonstrated to show metallic behavior, while zigzag and chiral nanotubes are semiconducting.¹⁶ In both cases, discrete valence and conduction band levels are formed with the distance between the highest valence band and the lowest conduction band level being higher in metallic CNTs than their semiconducting counterparts. Besides the interband transitions, a strong and broad $\pi - \pi^*$ plasmon absorption is expected in the ultraviolet (UV) spectral range, which slightly shifts for different polarization directions.¹⁶ Further, the conductivity in metallic and doped semiconducting CNTs will be observed as free-carrier absorption in the infrared spectral range. Much higher conductivity is observed along the CNT axes compared to the perpendicular direction.¹⁸

The polarization dependence of the interband transitions, the free-carrier absorption, and the $\pi - \pi^*$ plasmon, as well as their change with alignment, doping, and packing density of the nanotubes, determines the ranges of hyperbolic behavior in the dielectric function tensor in bulk effective mediums formed from the aligned CNT. The strongest optical anisotropy can be expected when all CNTs are aligned in one direction, resulting in effective uniaxial optical properties with the optical axis along the CNT axes and the ordinary dielectric function tensor component perpendicular to the CNT axes.¹⁹ The determination of the entire anisotropic dielectric function tensor requires advanced optical characterization techniques and measurement geometries. The polarization dependence of interband transitions in the aligned CNT has been studied in limited spectral ranges using polarized transmission,²⁰ polarized reflection,²¹ and polarized photoluminescence.²² Standard spectroscopic ellipsometry measurements were performed on horizontally but randomly aligned CNTs with in-plane isotropic optical properties.^{18,23–27} In this geometry, the anisotropy of the bulk effective medium is reduced due to averaging over all CNTs within the surface plane and only the tensor component perpendicular to the nanotube axes is uniquely defined. However, there is limited sensitivity to this so-called out-of-plane component of the dielectric function tensor (along the surface normal) in a reflection or transmission measurement even at oblique incidence and particularly in regions with absorption.²⁸

In this article, we describe the unambiguous determination of the uniaxial dielectric function tensor of bulk effective mediums formed from the aligned CNT. A multisample, multi-angle-of-incidence, and multiazimuth approach using Mueller matrix spectroscopic ellipsometry over the wide spectral range from the

mid-IR to the NIR-Vis-UV is applied to characterize the free-carrier, interband transitions, and $\pi - \pi^*$ -plasmon resonance related features perpendicular and along the CNT axes. Regions of hyperbolic dispersion are identified in the obtained dielectric function tensor and their shift with packing density and doping of the CNT films is discussed.

II. EXPERIMENT

The CNT films in this work were fabricated by the vacuum filtration method.^{3,5} A powder of arc-discharge single-walled CNTs with an average diameter of 1.41 nm was dispersed in water with the surfactant sodium dodecylbenzenesulfonate. The CNTs were not sorted and the solution contained approximately 1/3 metallic and 2/3 semiconducting CNT of an average length of 500 nm. A very weak vacuum then slowly pulled the suspension through a polycarbonate membrane causing the nanotubes to self-organize and align in the plane of the membrane. The membrane was then dried, and the one-inch-in-diameter CNT films were transferred to a silicon substrate. The filtration membranes for the vacuum filtration process (Whatman Nuclepore tracketched polycarbonate hydrophilic membranes, 0.05 μm pore size) were first treated with a 2 Torr air plasma for 30 s. This treatment provides a negative-charge surface on the membrane, which proved to be an important step for achieving a high degree of nanotube alignment and high packing density. Two different kinds of films were produced for this study: one of aligned but unordered CNTs and the other of aligned and ordered, i.e., hexagonally close-packed (“crystallized”) CNTs. The crystallinity of the CNT films was demonstrated before by means of transmission electron microscopy and x-ray diffraction.⁴ To study the optical properties in dependence of doping, we identify three distinct doping conditions. CNT films exposed to ambient conditions for an extended period of time (“ambient-doped”) are known to be unintentionally doped by adsorbates (e.g., water) resulting in small p-type conductivity.^{29,30} Minimally doped conditions are achievable by vacuum annealing.⁴ To induce strong p-type surface-charge-transfer doping, the crystallized film was exposed to HNO_3 vapor for 10 min. The doping level wears off slowly during exposure to atmospheric conditions. The ellipsometry measurements on the doped CNT film were performed about 24 h after the initial doping step when moderate doping levels still remain in the sample. A cross section transmission electron microscopy image and a top-view scanning electron microscopy image of the crystallized film are shown in Fig. 1.

Mueller matrix spectroscopic ellipsometry measurements at several angles of incidence and for a large number of sample azimuth orientations were obtained on a NIR-Vis-UV ellipsometer (J.A. Woollam Co. RC2 with an automated rotation stage, 193–1690 nm) and combined in a multisample analysis with data acquired on a mid-IR ellipsometer (J.A. Woollam Co. IR-VASE Mark II, 1.4–35 μm) at several angles of incidence and for measurement direction along, perpendicular, and 45° rotated with respect to the CNT axes. The NIR-Vis-UV ellipsometer is equipped with two rotating compensators and can access the entire Mueller matrix. Access to the full Mueller matrix allows for the calculation of the depolarization index,³¹ which was found to be >0.98 over the entire measured spectral range, indicating that depolarization

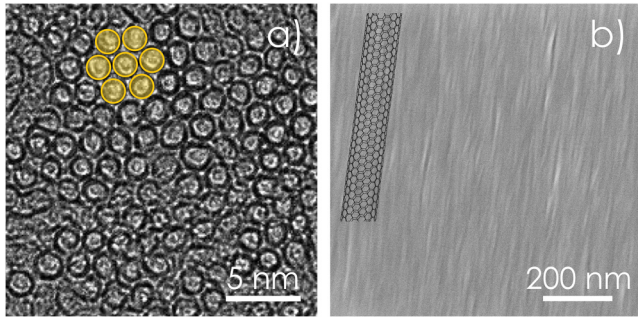


FIG. 1. Cross section transmission electron microscopy image (a) and top-view scanning electron microscopy image (b) for the crystallized film of single-walled CNTs. The hexagonal order and alignment direction are indicated by the sketches in the pictures.

effects minimally influence the measurements on the CNT films studied here. The mid-IR ellipsometer utilizes a single rotating compensator on the detector side and can access the first three columns of the Mueller matrix. Due to symmetry properties of the Mueller matrix and considering that depolarization can be neglected as indicated by the measurements on the NIR-Vis-UV ellipsometer, this is sufficient to fully characterize the anisotropic dielectric function tensor of the CNT films studied here. All datasets were combined and analyzed simultaneously using one optical model.

III. THEORY

We are determining the dielectric function tensor of our CNT films by spectroscopic ellipsometry in a reflection mode. For isotropic samples and uniaxial samples with the optical axis along the surface normal, no mode conversion for p-polarized light (within the plane of incidence) to s-polarized light (perpendicular to the plane of incidence) and vice versa occurs upon reflection, and the so-called standard ellipsometry formalism can be applied.³² In our case, all nanotubes and thus the optical axis of our bulk effective mediums are aligned parallel to the surface plane. Whenever the optical axis is not perfectly aligned parallel or perpendicular to the plane of incidence, mode conversion of s-polarized light to p-polarized light and vice versa occurs, and the so-called generalized ellipsometry formalism has to be applied.³² Here, either the entire Jones matrix must be measured (if the sample is nondepolarizing) or the Mueller matrix.³³ The Mueller matrix is the most general description of light interacting with a sample or an optical element, including depolarization and scattering effects, and connects the incoming Stokes vector S^{in} with the outgoing Stokes vector S^{out} ,

$$\begin{pmatrix} S_0 \\ S_1 \\ S_2 \\ S_3 \end{pmatrix}^{\text{out}} = \begin{pmatrix} M_{11} & M_{12} & M_{13} & M_{14} \\ M_{21} & M_{22} & M_{23} & M_{24} \\ M_{31} & M_{32} & M_{33} & M_{34} \\ M_{41} & M_{42} & M_{43} & M_{44} \end{pmatrix} \cdot \begin{pmatrix} S_0 \\ S_1 \\ S_2 \\ S_3 \end{pmatrix}^{\text{in}}, \quad (1)$$

with $S_0 = I_p + I_s$, $S_1 = I_p - I_s$, $S_2 = I_{+45^\circ} - I_{-45^\circ}$, and $S_3 = I_{\sigma^+} + I_{\sigma^-}$, where I_x refers to intensity measurements for p, s, $+45^\circ$, -45° , right-handed, and left-handed circular polarized light,

respectively. The offdiagonal blocks $M_{13}/M_{14}/M_{23}/M_{24}$ and $M_{31}/M_{32}/M_{41}/M_{42}$ are solely related to the cross-polarization reflection coefficients r_{sp} and r_{ps} .³³ Therefore, nonzero elements in these blocks indicate the presence of in-plane anisotropy in the sample. Measurements at multiple sample azimuths allow for characterization of a uniaxial dielectric function tensor with high sensitivity to both independent tensor elements and the orientation of the optical axis³² without prior assumptions.

Ellipsometry is an indirect technique and an appropriate optical model must be applied to extract the optical properties and layer thicknesses of the constituents of a sample consisting of layers on a substrate.³¹ Here, we set up a layer stack model in the CompleteEASE analysis software (J.A. Woollam Co.) consisting of an Si substrate, a layer for the bulk CNT film, and a surface roughness layer. The light propagation within the entire sample stack is calculated using a 4×4 transfer matrix algorithm for multilayer systems with plane-parallel interfaces similar to the formalism derived by Berreman.³⁴ A regression analysis (Levenberg-Marquardt algorithm) is performed where model parameters are varied until calculated and experimental data match as close as possible.³¹

The dielectric function tensor components of each sample constituent are needed as input for the transfer matrix formalism. The isotropic dielectric function for the Si substrate was taken without modification from the CompleteEASE library. The surface roughness layer was modeled by using the commonly applied Bruggeman effective medium approximation under the assumption of a 50:50 mixture of the CNT layer with air ($n = 1$).³¹ We are treating our films formed from aligned CNTs as bulk effective mediums with uniaxial optical properties. The corresponding dielectric function tensor in the material coordinate system is given by a diagonal tensor,

$$\boldsymbol{\varepsilon} = \mathbf{A} \begin{pmatrix} \varepsilon_{\perp} & 0 & 0 \\ 0 & \varepsilon_{\perp} & 0 \\ 0 & 0 & \varepsilon_{\parallel} \end{pmatrix} \mathbf{A}^{-1}, \quad (2)$$

with two distinct components ε_{\perp} and ε_{\parallel} , where “ \perp ” and “ \parallel ” denote polarization perpendicular and parallel to the axes of the aligned carbon nanotubes, respectively. Matrix \mathbf{A} is the Euler rotation matrix, which accounts for the orientation of the optical axis relative to the Cartesian laboratory coordinate system.³¹ In our case, the tilt angle θ rotates the optical axis into the surface plane ($\theta \approx 90^\circ$), and the azimuthal angle ϕ accounts for the orientation of the sample relative to the plane of incidence for each measurement. According to the theoretical predictions, we assume that the two distinct tensor elements are entirely independent.

In general, each of the two independent dielectric function tensor elements, ε_{\perp} and ε_{\parallel} , can be described as tabulated values for each photon energy (“point-by-point”), as interpolation functions of certain node spacing (B-splines³⁵), or can be modeled themselves using parameterized, energy-dependent algebraic functions—the model dielectric functions.³¹ These model dielectric functions describe a specific physical process in the material, such as an electronic interband transition, and are combined in order to render the overall spectral shape of a material’s dielectric function. We started with two independent sets of Kramers–Kronig-consistent B-spline functions to find the best match between the model and experimental data. The best-match B-spline functions were then used as a reference

to parameterize each dielectric function tensor element. The regression analysis on the experimental data was then repeated with the new set of parameterized model dielectric functions. A set of Gaussian oscillators was found to best describe the line shape of the interband transitions and the $\pi - \pi^*$ plasmon resonance,³⁶

$$\varepsilon_2(E) = A_n e^{-((E-E_n)/Br_n)^2} - A_n e^{-((E+E_n)/Br_n)^2}. \quad (3)$$

The variable parameters for each oscillator are the center energy E_n , the amplitude A_n , and the broadening Br_n . The real part is calculated using the Kramers–Kronig integration. The well-known Drude model is applied to match the free-carrier related absorption in the IR spectral range,³¹

$$\varepsilon(E) = \frac{-\hbar^2}{\varepsilon_0 \rho (\tau E^2 + i\hbar E)}. \quad (4)$$

The variable parameters for the Drude equation are the resistivity ρ given in Ω cm and the average scattering time τ in femtoseconds. A constant offset ε_∞ and a pole function account for any offset and dispersion in the real part of the dielectric function tensor

component due to absorption at higher energies outside the measured spectral range.³¹

IV. RESULTS AND DISCUSSION

An exemplary dataset of the Mueller matrix obtained for a 203 nm film of ambient-doped crystallized CNTs is shown in Fig. 2 for a photon energy of 0.73 eV. Experimental data for four angles of incidence (solid lines) and the best-matching model-calculated data (dotted lines) are shown for a full sample rotation. The data are bound between -1 and $+1$ due to normalization by the Mueller matrix element M_{11} (representative for total reflected unpolarized intensity). Note the excellent agreement between the model and the experiment for all rotation angles. A similar agreement was achieved over the entire measured spectral range from the mid-IR to the UV. Strong offdiagonal block elements indicate the highly anisotropic nature of these films. All Mueller matrix elements show a twofold symmetry indicated by the vertical markers in the second column in Fig. 2, which proves the effective uniaxial optical properties of the film. Four rotation angles can be identified where all offdiagonal block elements are identical to zero for all angles of incidence

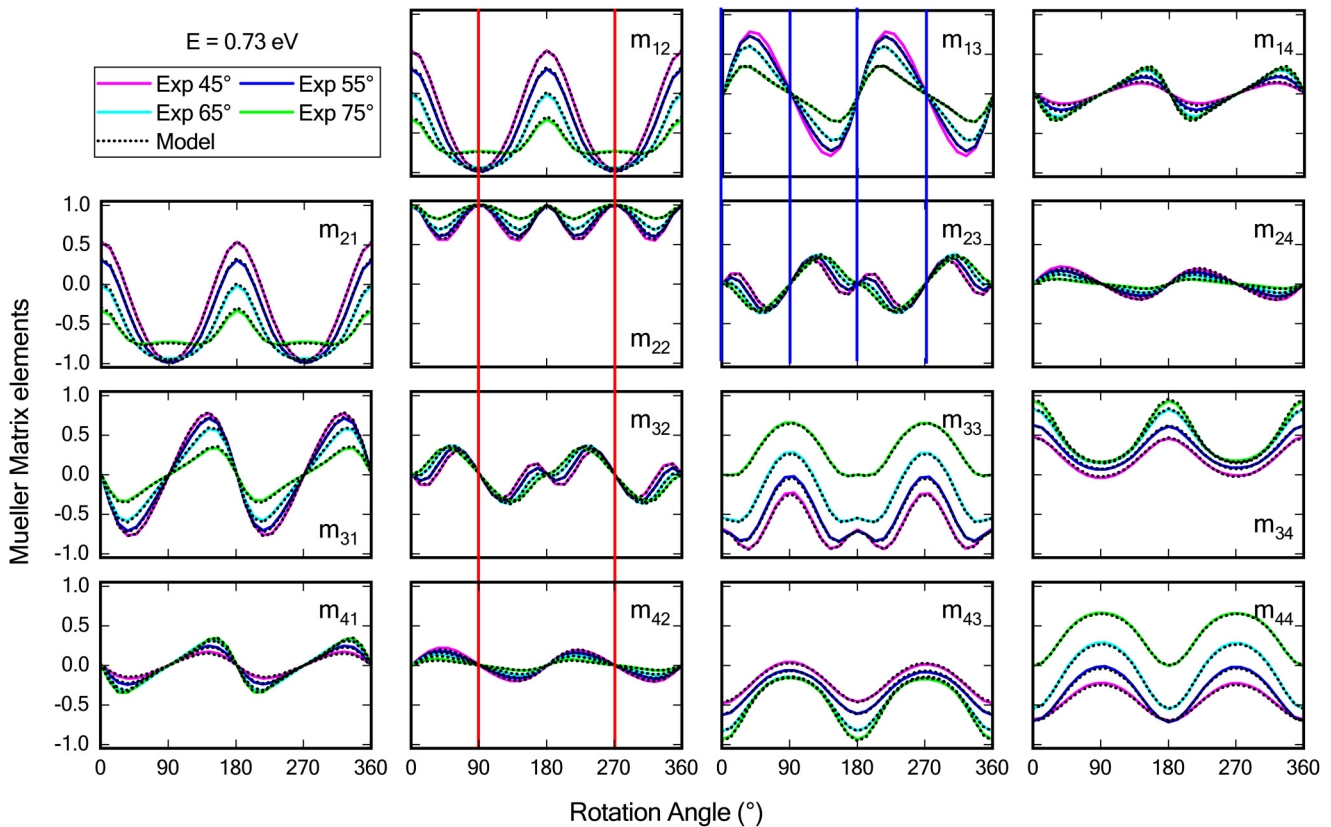


FIG. 2. Normalized Mueller matrix data obtained on the UV-Vis-NIR ellipsometer for a 203 nm film of ambient-doped crystallized CNTs. Experimental data for four angles of incidence (solid lines) as well as the best-matching model data (dotted lines) are shown for the exemplary energy of 0.73 eV for a full 360° rotation of the sample. Vertical lines in the second column show the twofold symmetry of all Mueller matrix elements, and vertical lines in m_{13} and m_{23} mark the pseudoisotropic orientations in the off-diagonal blocks.

(vertical lines in m_{13} and m_{23} in Fig. 2). These pseudoisotropic points prove that the optical axis is perfectly aligned in the surface plane as expected from the transmission electron microscopy images. From the spread of data vs the angle of incidence at $\phi = 0^\circ$, we can easily identify that the optical axis was within the plane of incidence at the beginning of the rotation scan even without a model analysis.

A uniaxial dielectric function tensor model was applied to match experimental and model data. A Kramers–Kronig-consistent B-spline model with 0.1 eV node spacing was used for each tensor element in order to obtain the best-matching model. The Euler angle θ was assumed to be identical for all datasets, while the azimuthal angle ϕ for the starting orientation of the full rotation scan in the NIR-Vis-UV spectral range and for each orientation of the mid-IR measurements was allowed to vary for each dataset. The thicknesses of the CNT layer and the surface roughness layer were varied during the regression analysis but assumed to be identical for all datasets. The two independent tensor elements of the best-matching model were then each parameterized with an appropriate number of Gaussian oscillators and a Drude absorption tail to account for free-carrier absorption in the IR spectral range. Eight Gaussian oscillators were necessary to match the parallel component of the dielectric function tensor and seven Gaussian oscillators for the perpendicular component. The purpose of the parameterization is to extract values for the physical quantities of average scattering time, resistivity, and the energies of the interband transitions and $\pi - \pi^*$ plasmon.³⁷ The line shape of the resulting dielectric function tensor components matches the B-spline extracted values nearly identically. Gaussian oscillators were chosen since they match the observed line shape well, and a Gaussian distribution of transition energies would be expected for normally distributed radii of CNT around the average radius.²⁴

Figure 3 shows the resulting dielectric function tensor elements for an ambient-doped sample of aligned but unordered CNTs. The most prominent features in the dielectric function tensor elements are due to electronic interband transitions and the broad $\pi - \pi^*$ plasmon absorption. In general, the absorption

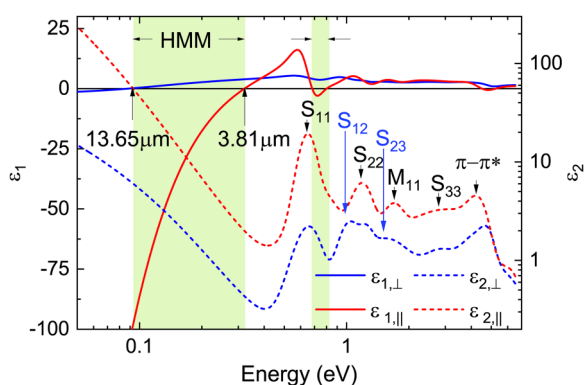


FIG. 3. Real part (ϵ_1) and imaginary part (ϵ_2) of the dielectric function tensor elements parallel and perpendicular to the CNT axes for an ambient-doped 40 nm film of aligned but not densely packed CNT. Known interband transitions and the $\pi - \pi^*$ plasmon absorption are marked by arrows. The hyperbolic ranges are indicated by shading.

features for polarization along the CNT axes are much stronger than that for the perpendicular direction (note the logarithmic scale for ϵ_2). Group theory predicts that for polarization along the CNT axis, optical transitions are only allowed between valence and conduction bands of an equal index, labeled S_{mn} for semiconducting CNTs and M_{mn} for metallic CNTs, where n is the band index. For polarization perpendicular to the CNT axes, only transitions between the valence band of index n and conduction bands of index $n \pm 1$ are expected. The strongest feature in the data located at 0.65 eV can be assigned to the transition from the first valence to the first conduction band in semiconducting CNT, S_{11} . The energetic position is consistent with theoretical predictions and experimental observations for CNTs of this diameter.^{14,18,24} Note that the absorption is expected to be caused by excitons located slightly below the actual band-to-band transition energy but it is not possible to distinguish between exciton and band-to-band absorption using the ellipsometry technique. The next higher allowed transition S_{22} is found at 1.18 eV again in agreement with earlier publications.^{14,18,24} Since the films contain a mix of semiconducting and metallic CNTs, we can also identify the transition from the first valence to the conduction band in metallic structures, M_{11} , in our data. This transition is located at 1.67 eV. A broad absorption peak is observed in the range where S_{33} and S_{44} are expected. The broad $\pi - \pi^*$ plasmon absorption is located at 4.32 eV for this polarization. A narrow distribution of CNT diameters in our mix of CNTs can be concluded from the existence of relatively narrow and clearly defined peaks for the interband transitions.²⁷ Despite the selection rules, for polarization perpendicular to the CNT axes, we can identify the same peaks as for the parallel component but with a much weaker amplitude. This is likely related to a slight misalignment of the nanotubes in this unordered film. In addition, we can identify two peaks that can be assigned to the symmetry-allowed interband transitions S_{12}/S_{21} and S_{23}/S_{32} . Even these allowed transitions are much smaller in amplitude than the strong interband absorptions for polarization along the CNT axes. Local field effects have to be taken into account to correctly describe the amplitude of absorption relative to the CNT axes.^{12,15} A depolarization effect leads to strongly reduced electronic transitions for light polarized perpendicular to the CNT axes compared to polarization along the CNT axes resulting in very sharp and strong features for absorption measurements with polarization parallel to the nanotube axes and much smaller and very broad absorption for polarization perpendicular to the nanotube axes.¹⁶ Intertube interactions can strongly modify the depolarization effect.^{15–17} The broad $\pi - \pi^*$ plasmon absorption for polarization perpendicular to the CNT axes is located at 4.79 eV, which is slightly higher than for polarization along the CNT axes in agreement with theoretical predictions.¹⁶

The hyperbolic ranges in the dielectric function tensor of aligned but unordered CNTs are marked by shading in Fig. 3. A very wide range of hyperbolic dispersion between 3.81 and 13.65 μm is found. This range is mainly caused by the large difference in conductivity along the CNT axes and perpendicular to the CNT axes. The values for the resistivity obtained from the Drude model are $\rho_{\parallel} = 3.0 \times 10^{-4} \Omega \text{ cm}$ along the CNT axes and $\rho_{\perp} = 8.6 \times 10^{-3} \Omega \text{ cm}$ perpendicular to the CNT axes. The relatively low resistivities in these ambient-doped films are caused by the metallic CNT and ambient p-type doping in the

semiconducting CNT. For films of purely semiconducting CNTs, we would expect a shift of the hyperbolic range toward longer wavelengths. Average scattering times of $\tau_{\parallel} = 13.8$ fs and $\tau_{\perp} = 5.2$ fs are consistent with the picture of reduced conductivity perpendicular to the CNT axes. It has been demonstrated that the resistivity parameters obtained from contactless ellipsometry measurements agree within 6% with electrical point probe measurements in these films.²⁶

The obtained dielectric function tensor elements for a CNT sample of aligned and ordered (crystalline) CNTs are presented in Fig. 4. Both ambient-doped and highly doped CNT films are shown. Compared to the unordered CNT film, the dielectric function tensor component parallel to the CNT axes is essentially unchanged for the ambient-doped film [Fig. 4(a)]. For the perpendicular direction, the contribution of transitions assigned to parallel polarization is strongly reduced while the S_{12}/S_{21} and S_{23}/S_{32} transitions can still clearly be identified. This indicates the close to perfect alignment of the CNT in this sample. The width of the hyperbolic spectral range is slightly reduced due to a reduced resistivity of $\rho_{\perp} = 4.1 \times 10^{-3} \Omega \text{ cm}$ and an increased average scattering time of $\tau_{\perp} = 11.1$ fs, indicating better conductivity perpendicular to the

CNT axes in the ordered film compared to the unordered case. Further, an additional small and very broad absorption feature appears in the mid-IR spectral range [indicated by the upwards pointing arrow in Fig. 4(a)]. The nature of this absorption feature is not entirely clear and could be related to a plasmon absorption related to the domain size of perfectly ordered CNTs (approximately 25 nm in this sample), infrared absorption of covalently bound functional groups,²⁷ or some other effects. Note that the amplitude of this absorption feature is relatively small and only marginally influences the obtained results.

For the doped film [Fig. 4(b)], a very different picture arises. The hyperbolic spectral range is shifted significantly toward shorter wavelengths. This strong shift is a consequence of reduced resistivity for both dielectric function tensor components. Resistivity values of $\rho_{\parallel} = 1.1 \times 10^{-4} \Omega \text{ cm}$ along the CNT axes and $\rho_{\perp} = 2.1 \times 10^{-3} \Omega \text{ cm}$ perpendicular to the CNT axes are obtained while the scattering times of $\tau_{\parallel} = 11.8$ fs and $\tau_{\perp} = 9.6$ fs are not changed much from the ambient-doped case. This implies that the Fermi level was lowered within the CNT, which resulted in a higher hole concentration, while the mobility of the carriers remains mainly unchanged. This picture is consistent with the observed behavior of the interband transitions. The strongest transition from the first valence to the first conduction band, S_{11} , nearly vanishes in the doped case. This can be explained by a drop of the Fermi level below the first valence band and the resulting hole saturation which does not allow further transitions between this band and the first conduction band. The reduction of this transition essentially connects the two hyperbolic ranges observed in the ambient-doped case as a result of the absence of the derivative-like structure in ϵ_1 caused by the strong S_{11} absorption. For polarization perpendicular to the CNT axes, an additional absorption feature arises below the S_{12}/S_{21} transition. This transition, S_{41} , can be assigned to an intervalence band transition, which occurs due to modified selection rules of the optical transitions at very high doping levels.⁴ The absorption feature related to the S_{12}/S_{21} transition is slightly reduced compared to the ambient-doped case due to the hole saturation of the first valence band while the second valence band remains only partially filled. Note that the energy gap between the first valence band and the second conduction band and the energy gap between the second valence band and the first conduction band are nearly identical.²⁴ We expect that even higher doping concentrations can be achieved which would further shift the hyperbolic range to shorter wavelengths.

V. CONCLUSION

We have demonstrated a reliable approach to characterize the uniaxial dielectric function tensor of aligned CNT films by using Mueller matrix ellipsometry. Measurements at many sample orientations and angles of incidence were performed over the very wide spectral range from the mid-IR to UV. The resulting dielectric function tensor elements were parameterized using a combination of Gaussian oscillators to describe the electronic interband transitions and the $\pi - \pi^*$ plasmon absorption. A Drude absorption tail accounts for the free-carrier absorption in the mid-IR and allows for the determination of the resistivity and average scattering time contactlessly. The observed interband transitions were identified

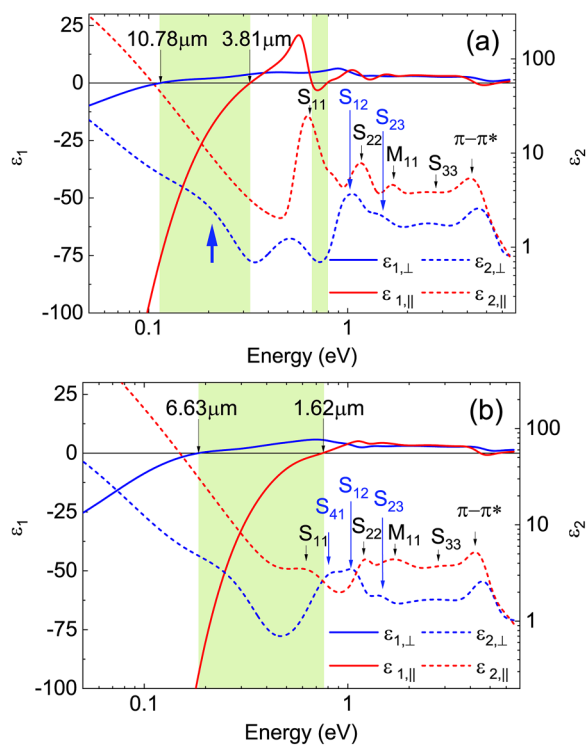


FIG. 4. Real part (ϵ_1) and imaginary part (ϵ_2) of the dielectric function tensor elements parallel and perpendicular to the CNT axes for a 208 nm film of aligned and densely packed (crystalline) CNTs for the ambient-doped case (a) and the highly doped case after exposure to HNO_3 vapor (b). Known interband transitions and the $\pi - \pi^*$ plasmon absorption are marked by arrows. The hyperbolic ranges are indicated by shading. An additional small absorption in the mid-IR spectral range is marked with a upward-pointing arrow.

by comparison with theoretical predictions and prior experimental results. We showed that aligned films of CNTs exhibit wide ranges of hyperbolic dispersion in the NIR and mid-IR spectral range suitable for many device applications. The existence of the hyperbolic spectral range can be explained by the large discrepancy in the resistivity in the films along the CNT axes and perpendicular to it as indicated by the shift in the Drude absorption tail and by strongly reduced amplitudes of the electronic interband transitions for polarization along and perpendicular to the CNT axes. Consequently, the hyperbolic range can be tuned over a remarkably wide range by modifying the Fermi level in the films, for example, through doping by exposure to HNO₃ vapor, and by fine-tuning the composition and alignment of the nanotubes. We demonstrated this by comparing the dielectric function tensor of an aligned but unordered CNT film with results obtained on a film of aligned and densely packed (crystalline) CNTs in an ambient-doped and a doped case. Metamaterials formed from aligned CNTs are thus a promising route to achieve tunable hyperbolic behavior.

REFERENCES

- ¹P. Shekhar, J. Atkinson, and Z. Jacob, "i/DIFdel, *Nano Converg.* **1**, 14 (2014).
- ²A. Poddubny, I. Iorsh, P. Belov, and Y. Kivshar, *Nat. Photonics* **7**, 948 (2013).
- ³X. He, *et al.*, *Nat. Nanotechnol.* **11**, 633 (2016).
- ⁴P.-H. Ho, D. B. Farmer, G. S. Tulevski, S.-J. Han, D. M. Bishop, L. M. Gignac, J. Bucchignano, P. Avouris, and A. L. Falk, *Proc. Natl. Acad. Sci. U.S.A.* **115**, 12662 (2018).
- ⁵J. A. Roberts, S.-J. Yu, P.-H. Ho, S. Schoeche, A. L. Falk, and J. A. Fan, *Nano Lett.* **19**, 3131 (2019).
- ⁶W. A. DeHeer, W. Bacsá, A. Chatelain, T. Gerfin, R. Humphrey-Baker, L. Forro, and D. Ugarte, "i/DIFdel, *Science* **268**, 845 (1995).
- ⁷F. Bommeli, L. Degiorgi, P. Wachter, W. Bacsá, W. A. de Heer, and L. Forro, *Solid State Commun.* **99**, 513 (1996).
- ⁸T. de Los Arcos, P. Oelhafen, and D. Mathys, *Nanotechnology* **18**, 265706 (2007).
- ⁹T. Barnes, *et al.*, *Phys. Rev. B* **75**, 235410 (2007).
- ¹⁰F. Garcia-Vidal, J. Pitarke, and J. Pendry, *Phys. Rev. Lett.* **78**, 4289 (1997).
- ¹¹W. Lü, J. Dong, and Z.-Y. Li, *Phys. Rev. B* **63**, 033401 (2000).
- ¹²H. Ajiki and T. Ando, *Jpn. J. Appl. Phys.* **34**, 107 (1995).
- ¹³S. Uryu and T. Ando, *Phys. Rev. B* **74**, 155411 (2006).
- ¹⁴I. Milošević, T. Vuković, S. Dmitrović, and M. Damjanović, *Phys. Rev. B* **67**, 165418 (2003).
- ¹⁵A. Marinopoulos, L. Reining, A. Rubio, and N. Vast, *Phys. Rev. Lett.* **91**, 046402 (2003).
- ¹⁶G. Guo, K. Chu, D.-S. Wang, and C.-G. Duan, *Phys. Rev. B* **69**, 205416 (2004).
- ¹⁷G. Zhao, D. Bagayoko, and L. Yang, *J. Appl. Phys.* **99**, 114311 (2006).
- ¹⁸M. M. Junda, A. B. Phillips, R. R. Khanal, M. J. Heben, and N. J. Podraza, *Carbon* **129**, 592 (2018).
- ¹⁹Bulk films of horizontal but randomly oriented CNT also show uniaxial optical properties, but due to the averaging of the optical response of all CNT within the surface plane, the optical axis will point along the surface normal and the ordinary component represents an average of the optical response parallel and perpendicular to the CNT axis.
- ²⁰J. Fagan, *et al.*, *Phys. Rev. Lett.* **98**, 147402 (2007).
- ²¹J. Hwang, H. Gommans, A. Ugawa, H. Tashiro, R. Haggenmueller, K. I. Winey, J. E. Fischer, D. Tanner, and A. Rinzler, *Phys. Rev. B* **62**, R13310 (2000).
- ²²J. Lefebvre and P. Finnie, *Phys. Rev. Lett.* **98**, 167406 (2007).
- ²³G. Fanchini, S. Miller, B. B. Parekh, and M. Chhowalla, "i/DIFdel, *Nano Lett.* **8**, 2176 (2008).
- ²⁴Y. Battie, D. Jamon, J.-S. Lauret, A. E. Naciri, L. Broch, and A. Loiseau, *Carbon* **50**, 4673 (2012).
- ²⁵Y. Battie, D. Jamon, A. En Naciri, J.-S. Lauret, and A. Loiseau, *Appl. Phys. Lett.* **102**, 091909 (2013).
- ²⁶Y. Battie, L. Broch, A. E. Naciri, J.-S. Lauret, M. Guézo, and A. Loiseau, *Carbon* **83**, 32 (2015).
- ²⁷Y. Battie, M. Dossot, N. Allali, V. Mamane, A. E. Naciri, L. Broch, and A. V. Soldatov, *Carbon* **96**, 557 (2016).
- ²⁸D. Aspnes, *JOSA* **70**, 1275 (1980).
- ²⁹P. G. Collins, K. Bradley, M. Ishigami, and D. A. Zettl, *Science* **287**, 1801 (2000).
- ³⁰A. Zahab, L. Spina, P. Poncharal, and C. Marliere, *Phys. Rev. B* **62**, 10000 (2000).
- ³¹H. Fujiwara, *Spectroscopic Ellipsometry: Principles and Applications* (Wiley, New York, 2007).
- ³²M. Schubert, "Theory and application of generalized ellipsometry," in *Handbook of Ellipsometry*, edited by E. A. Irene and H. G. Tompkins (William Andrew, New York, 2004).
- ³³R. M. A. Azzam and N. M. Bashara, *Ellipsometry and Polarized Light* (North-Holland, Amsterdam, 1977).
- ³⁴D. W. Berreman, *J. Opt. Soc. Am.* **62**, 502 (1972).
- ³⁵B. Johs and J. S. Hale, *Phys. Status Solidi A* **205**, 715 (2008).
- ³⁶D. D. S. Meneses, M. Malki, and P. Echegut, *J. Non-Cryst. Solids* **352**, 769 (2006).
- ³⁷The actual values of broadening and amplitudes are irrelevant for the discussion in this paper and are omitted for brevity.